The Major-Element Composition of Mercury's Surface from MESSENGER X-ray Spectrometry

Larry R. Nittler, *et al.*

Science **333**, 1847 (2011);
DOI: 10.1126/science.1211567

This copy is for your personal, non-commercial use only.

If you wish to distribute this article to others, you can order high-quality copies for your colleagues, clients, or customers by clicking here.

Permission to republish or repurpose articles or portions of articles can be obtained by following the guidelines here.

The following resources related to this article are available online at www.sciencemag.org (this infomation is current as of September 29, 2011):

Updated information and services, including high-resolution figures, can be found in the online version of this article at:
http://www.sciencemag.org/content/333/6051/1847.full.html

Supporting Online Material can be found at:
http://www.sciencemag.org/content/suppl/2011/09/28/333.6051.1847.DC1.html
http://www.sciencemag.org/content/suppl/2011/09/29/333.6051.1847.DC2.html

This article **cites 49 articles**, 11 of which can be accessed free:
http://www.sciencemag.org/content/333/6051/1847.full.html#ref-list-1

This article has been **cited by** 4 articles hosted by HighWire Press; see:
http://www.sciencemag.org/content/333/6051/1847.full.html#related-urls

Downloaded from www.sciencemag.org on September 29, 2011

Science (print ISSN 0036-8075; online ISSN 1095-9203) is published weekly, except the last week in December, by the American Association for the Advancement of Science, 1200 New York Avenue NW, Washington, DC 20005. Copyright 2011 by the American Association for the Advancement of Science; all rights reserved. The title *Science* is a registered trademark of AAAS.

The Major-Element Composition of Mercury's Surface from MESSENGER X-ray Spectrometry

Larry R. Nittler,[1]* Richard D. Starr,[2] Shoshana Z. Weider,[1] Timothy J. McCoy,[3] William V. Boynton,[4] Denton S. Ebel,[5] Carolyn M. Ernst,[6] Larry G. Evans,[7] John O. Goldsten,[6] David K. Hamara,[4] David J. Lawrence,[6] Ralph L. McNutt Jr.,[6] Charles E. Schlemm II,[6] Sean C. Solomon,[1] Ann L. Sprague[4]

X-ray fluorescence spectra obtained by the MESSENGER spacecraft orbiting Mercury indicate that the planet's surface differs in composition from those of other terrestrial planets. Relatively high Mg/Si and low Al/Si and Ca/Si ratios rule out a lunarlike feldspar-rich crust. The sulfur abundance is at least 10 times higher than that of the silicate portion of Earth or the Moon, and this observation, together with a low surface Fe abundance, supports the view that Mercury formed from highly reduced precursor materials, perhaps akin to enstatite chondrite meteorites or anhydrous cometary dust particles. Low Fe and Ti abundances do not support the proposal that opaque oxides of these elements contribute substantially to Mercury's low and variable surface reflectance.

Elemental abundances at the surface of a rocky planet reflect the composition of the original materials from which the planet formed, as well as the accretion, differentiation, impact, and geological processes that have shaped the surface over billions of years. Before the MESSENGER mission (*1*), constraints on the composition of Mercury were indirect and included a high overall metal/silicate ratio (inferred from the planet's bulk density), low FeO in surface silicates, and the presence of K, Na, Ca, and other elements in the planet's exosphere (*2*–*5*). Several models of Mercury's origin and early evolution were developed to explain the high metal/silicate ratio, including sorting of metal and silicate particles in the early solar nebula by thermal or physical processes before planetary accretion (*6*, *7*), evaporation of an outer silicate crust and mantle by a hot early solar nebula (*8*), and removal of large portions of the outer silicate fraction of a differentiated planet by a giant impact (*9*, *10*). These models led to a variety of predictions for the composition of surface materials on Mercury (*11*). The MErcury Surface, Space ENvironment, GEochemistry, and Ranging (MESSENGER) spacecraft, in orbit around Mercury since 18 March 2011, includes an X-Ray Spectrometer (XRS), which makes direct measurements of the surface abundances of the key rock-forming elements: Mg, Al, Si, S, Ca, Ti, and Fe. Here, we discuss XRS observations of Mercury's surface chemistry from the first 90 days of MESSENGER orbital science operations.

The MESSENGER XRS (*12*, *13*) detects fluorescent x-ray emissions, induced by solar x-rays, from the top tens of micrometers of Mercury's surface. It consists of three planet-facing gas-filled proportional counters (GPCs), which detect fluorescent and scattered solar x-rays with energies of 1 to 10 keV. Thin foils of Mg and Al in front of two of the detectors allow deconvolution of the fluorescent signals from the geochemically important elements Mg, Al, and Si. Spatial resolution for a single spectral measurement depends on spacecraft altitude and integration time and ranges from <50 km to >3000 km (*13*).

The solar x-ray spectrum is highly variable in time, strongly affecting the strength and shape of x-ray spectra observed from Mercury's surface. The XRS thus also includes a Sun-facing detector (Solar Assembly for X-rays, or SAX) to simultaneously measure incident solar x-ray spectra (*12*). During typical solar conditions, XRS detects fluorescent signals only from Mg, Al, and Si. However, the solar flux is greatly enhanced during flares, especially at higher energies, allowing detection of elements with atomic numbers up to that of Fe. Here, we focus on data acquired during solar flares because these provide the most geochemical information.

We used a forward modeling approach to convert observed spectra to elemental abundances (*13*). For a given observation, a theoretical solar plasma spectrum was fit to the observed SAX spectrum and used, along with the appropriate observation geometry (incidence, emission, and phase angles) and an assumed composition, to calculate theoretical XRS spectra (*13*–*15*). Elemental abundances were varied in a nonlinear least-squares fitting procedure until the best match to the observed spectra was obtained. We discuss abundance ratios relative to silicon because these are more accurately determined than absolute abundances.

Most of the data reported here (Table 1) were acquired at high altitude, when the instrument's field of view projected onto the planet's surface (or its footprint) was large, and hence represent averages over large areas of the surface (Fig. 1). The measured footprints are primarily located in the southern hemisphere, between longitudes of about −180° and −60°E. Low-altitude data from one flare (on 16 April 2011) have smaller footprints and include one region of northern volcanic smooth plains (*16*).

Mercury has a higher Mg/Si ratio and lower Al/Si and Ca/Si ratios than the terrestrial and lunar crusts (Fig. 2), indicating a lower abundance of plagioclase feldspar, a common crustal mineral. Mercury's ratios are intermediate between typical basaltic compositions and more ultramafic compositions comparable to terrestrial komatiites. The derived compositions are reasonably close to those estimated from mineral assemblages inferred from ground-based infrared spectral data (*17*, *18*).

All analyzed flare spectra unambiguously show the presence of abundant sulfur. The S/Si ratios range from ~0.05 to 0.15. An O abundance inferred from the usual stoichiometry of the major cations implies an average surface Si abundance of ~25 weight % (wt %) and hence an S abundance of up to ~4 wt % in surface materials. This concentration is much higher than observed in the bulk silicate Earth, lunar silicates, or stony meteorites from Mars and differentiated asteroids, the S content for all of which are estimated to be $\lesssim$ 0.2 wt %. The low S abundances on these objects are thought to reflect loss of volatiles during planet formation and/or sequestration into planetary cores. Higher S abundances, comparable to those reported here, have been measured in situ on the surfaces of Mars and Venus, but those instances likely are the result of aqueous processing and surface-atmospheric interaction, respectively (*19*, *20*).

Data from the most intense flares (*13*) reveal that Mercury's surface is low in Ti and Fe. Derived Ti/Si ratios range from 0.007 to 0.03, and Fe/Si ratios range from 0.01 to 0.15, giving upper limits on absolute abundances of ~0.8 wt % for Ti and ~4 wt % for Fe. Analysis of the highest signal-to-noise XRS spectra also provided upper limits of ~0.2% for Cl and ~0.5 wt % for Cr and Mn (*13*).

Mercury's relatively low Al/Si and Ca/Si ratios rule out the presence of a plagioclase-rich crust similar to that of the lunar highlands. The latter is thought to have formed by flotation of crystallized plagioclase-rich rocks that solidified

---

[1]Department of Terrestrial Magnetism, Carnegie Institution of Washington, Washington, DC 20015, USA. [2]Physics Department, The Catholic University of America, Washington, DC 20064, USA. [3]Smithsonian Institution, Washington, DC 20013, USA. [4]Lunar and Planetary Laboratory, University of Arizona, Tucson, AZ 85721, USA. [5]Department of Earth and Planetary Science, American Museum of Natural History, New York, NY 10024, USA. [6]The Johns Hopkins University Applied Physics Laboratory, Laurel, MD 20723, USA. [7]Computer Sciences Corporation, Lanham-Seabrook, MD 20706, USA.

*To whom correspondence should be addressed. E-mail: lnittler@ciw.edu

Table 1. Elemental abundances derived for Mercury's surface from XRS observations during 10 solar flares. The flare on 16 April was divided into two time segments for independent analysis (nos. 1 and 2). Mg/Si, Al/Si, S/Si, and Ca/Si ratios are means and standard deviations of individual integrations for each flare. Errors incorporate systematic errors due to uncertain solar spectra fitting. Ti/Si and Fe/Si are derived ratios and statistical errors for highest signal-to-noise spectrum for a given flare. The second segment of the 16 April flare was analyzed as a single summed spectrum; derived ratios and statistical errors are shown.

Flare no.	Date and start time (UTC)	Total integration time (s)	Max. solar temp. (10^6 K)	Mg/Si	Al/Si	S/Si	Ca/Si	Ti/Si	Fe/Si
1	16 April 2011 16:40:41	705	13.2	0.62 ± 0.04	0.19 ± 0.03	0.14 ± 0.02	0.30 ± 0.06		
2	16 April 2011 16:53:06	80	8.6	0.33 ± 0.03	0.22 ± 0.05	0.08 ± 0.02			
3	22 April 2011 1:26:13	3600	11.5	0.50 ± 0.07	0.24 ± 0.02	0.09 ± 0.01	0.20 ± 0.04		
4	22 April 2011 4:56:47	2319	17.3	0.58 ± 0.04	0.17 ± 0.02	0.15 ± 0.02	0.29 ± 0.03	<0.01	0.03 ± 0.02
5	22 April 2011 17:01:00	909	14.6	0.67 ± 0.08	0.18 ± 0.01	0.15 ± 0.01	0.30 ± 0.03	0.010 ± 0.004	0.06 ± 0.01
6	1 May 2011 23:22:43	900	16.1	0.41 ± 0.03	0.25 ± 0.005	0.07 ± 0.01	0.21 ± 0.003	0.007 ± 0.003	0.12 ± 0.01
7	15 May 2011 23:24:02	2250	13.4	0.43 ± 0.09	0.28 ± 0.03	0.07 ± 0.005	0.22 ± 0.01	0.03 ± 0.01	0.15 ± 0.01
8	13 June 2011 3:53:14	900	16.5	0.39 ± 0.04	0.26 ± 0.004	0.05 ± 0.002	0.15 ± 0.01	0.007 ± 0.001	0.05 ± 0.01
9	14 June 2011 21:44:36	2250	15.6	0.36 ± 0.06	0.26 ± 0.01	0.06 ± 0.01	0.18 ± 0.01		
10	16 June 2011 10:19:05	2250	14.2	0.53 ± 0.03	0.27 ± 0.004	0.07 ± 0.01	0.17 ± 0.02	<0.01	0.08 ± 0.01
11	16 June 2011 11:56:46	800	11.8	0.64 ± 0.06	0.28 ± 0.02	0.07 ± 0.01	0.18 ± 0.02		

from a global magma ocean (*21*). It is not known whether Mercury also experienced a magma ocean stage in its early history. Magma ocean models [e.g., (*21*, *22*)] predict that the formation of a flotation crust depends strongly on the planet's bulk silicate composition. For FeO abundances less than a few percent in the bulk silicate fraction of the planet, crystallizing plagioclase will not float in the coexisting magma. In such a case, the final surface composition would likely be dominated by lava flows formed from the subsequent partial melting of mantle material solidified during magma ocean cooling. The low surface Fe abundance as measured by XRS confirms a low total FeO abundance in Mercury's mantle (*23*) and therefore suggests that a plagioclase flotation crust never formed. The observed compositions are also inconsistent with some predictions (*22*) for remelting of magma ocean solidification products (Fig. 2), but only a limited set of starting compositions has been considered in these models to date.

The derived Mg/Si, Al/Si, and Ca/Si ratios indicate a surface composition depleted in plagioclase relative to compositions characteristic of early melts from an Earth-like mantle (e.g., oceanic basalts). This result might suggest removal of an early basaltic crust by either large-scale evaporation (*8*) or giant impact events (*9*, *10*). However, neither model is supported by mounting evidence that Mercury is not highly depleted in volatile elements relative to the other terrestrial planets (*24*). A more likely scenario is that Mercury's unusual metal-rich, FeO-poor composition reflects the primary nature of its precursor materials. Early hypotheses (*6*) that Mercury formed primarily from high-temperature materials that condensed at equilibrium in the innermost solar system predicted high abundances of refractory elements such as Ca and Al and low abundances of volatile elements such as S and K. Such refractory-rich, volatile-poor compositions are ruled out by the elemental

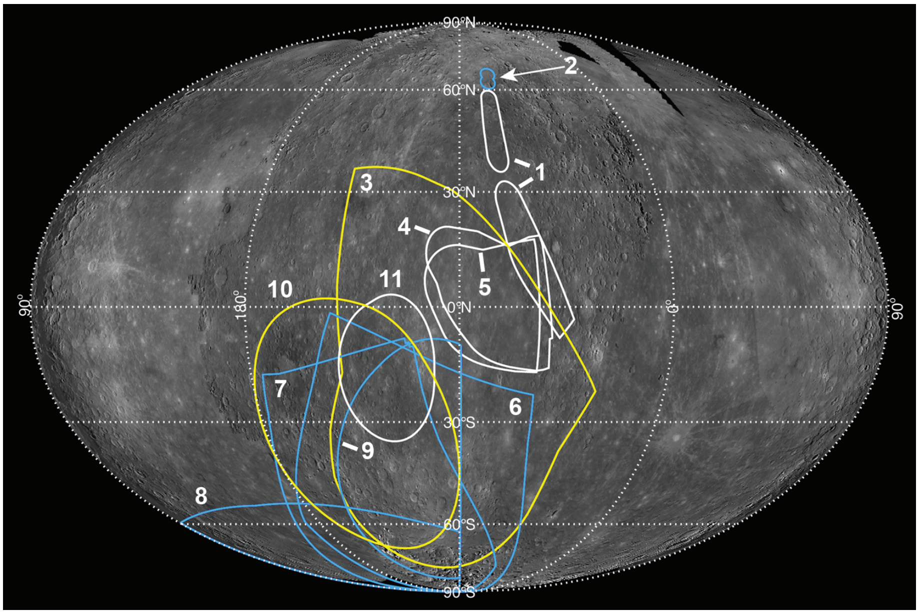

Fig. 1. Regions of Mercury (footprints) sampled by XRS during analyzed flares, numbered according to Table 1. Outline colors reflect derived Mg/Si ratios: white, Mg/Si ≈ 0.6; yellow, Mg/Si ≈ 0.5; blue, Mg/Si ≈ 0.4. Arrow indicates spatially resolved measurement of a portion of northern plains material (*16*).

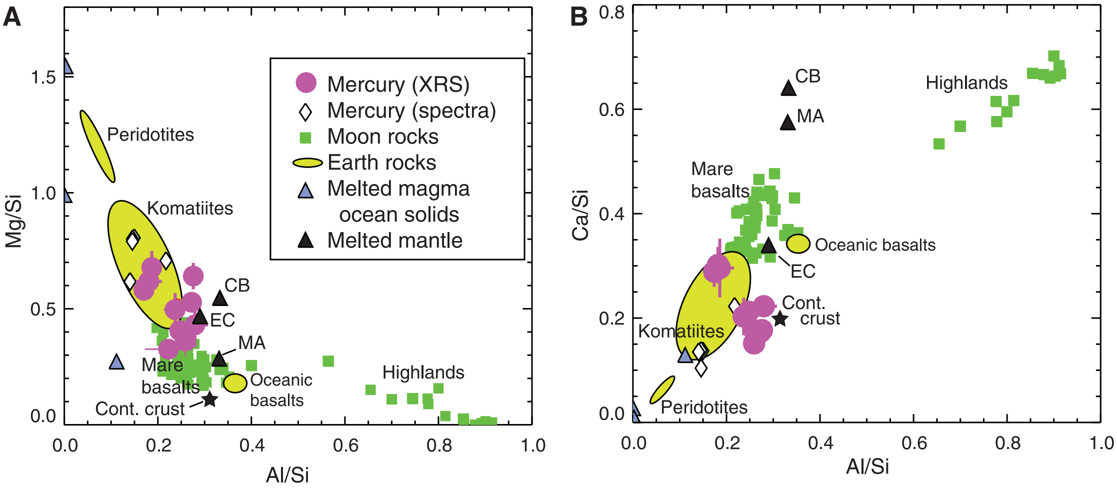

Fig. 2. (**A** and **B**) Mg/Si, Al/Si, and Ca/Si mass ratios for Mercury (Table 1) compared with terrestrial (*35*) and lunar (*36*) compositions and predicted Mercury compositions. Mercury (spectra) denotes compositions inferred from ground-based infrared spectra (*17*, *18*). Also shown are predictions of partially melted magma ocean products (*22*), partially melted CB chondrite composition (*11*), partially melted EC (*26*, *27*), and partial melts (*11*) from a mix of refractory and volatile materials (MA) (*25*).

abundances reported here. More recent ideas focus on accreting Mercury from mixtures of refractory-enriched and Earth-like compositions (*11*, *25*) or highly reduced (*26*) and/or metal-rich (*22*) chondritic meteorite compositions (enstatite and/or CB chondrites, respectively). We compared the XRS results with Mg/Si, Al/Si, and Ca/Si ratios predicted for partial melting of material of these compositions (as proxies for surface lava flows) (Fig. 2). Of these compositions, only the partially melted enstatite chondrite (EC) composition is reasonably similar to the observations, although not a perfect match. This composition is also enriched in S (*26*), at about the same level that we observe on Mercury. This is because, under highly reducing conditions, substantial S is incorporated into silicate melts (*27*), unlike the situation under more oxidizing conditions.

The low Fe abundance indicates that the surface S cannot be present primarily in the form of iron sulfides. More likely the S occurs in Mg- and/or Ca-rich sulfides, which are stable under reducing conditions and present in highly reduced enstatite chondrite and aubrite meteorites. Their presence on Mercury has been previously suggested on the basis of ground-based observations (*28*) and is supported by a general correlation among Mg/Si, Ca/Si, and S/Si ratios observed here (*13*) (fig. S8). Magmas coexisting with these sulfides would have extremely low FeO contents (<1 wt %) (*25*). Moreover, the high abundance of S, if it can be extrapolated to Mercury's interior, could potentially provide an abundant source of volatile gases to drive pyroclastic volcanism on Mercury (*29*, *30*).

Mercury's geologic evolution has shaped a surface that likely contains materials varying in composition and depths of origin (*31*, *32*). It is therefore unrealistic to expect the surface composition to match precisely the predictions of a single-stage episode of partial melting from a primitive mantle. Nonetheless, the similarity of the observed average composition to that predicted by simple partial melting of an EC-like composition, especially the high S abundance, strongly suggests that Mercury indeed formed preferentially from highly reduced, but not strongly volatile-depleted, precursors. However, ECs have insufficiently high bulk Fe/Si ratios to explain Mercury's high density without an additional step of metal/silicate fractionation in the solar nebula or silicate removal by giant impact. It is also unlikely that the primitive extraterrestrial materials studied today completely sample the range of building blocks from which the terrestrial planets accreted. It is possible that EC-like objects with higher metal abundances were present in the early inner solar system. Alternatively, Mercury may have been built from solids condensed in ice-poor systems enriched in anhydrous interplanetary dust particles (*33*). These particles, likely derived from comets, are also highly reduced.

Data acquired by MESSENGER during its three flybys of Mercury in 2008–2009 revealed the presence of distinct terrains with subtle differences in color and reflectance that are suggestive of differing chemical compositions (*28*, *29*). In particular, color and reflectance observations have been interpreted in terms of a variable contribution from comparatively dark, spectrally neutral material, and suggested candidate opaque minerals include Fe- and Ti-bearing oxides and/or sulfides. Moreover, flyby data from MESSENGER's Neutron Spectrometer (*34*) indicate a neutron-absorption cross section similar to that of several lunar mare soils, for which the neutron absorption is dominated by a combination of Fe and Ti. This result supported the suggestion that Fe-Ti oxides may be in high abundance on Mercury, despite the low amount of FeO in the surface silicates. The low Fe and Ti abundances inferred from the XRS data, however, do not support a high abundance of such oxides on the surface and require that additional element(s) are responsible for the high observed neutron-absorption cross section. Observed abundances or abundance limits on S, Fe, Cl, Ti, and/or Mn are consistent with the lower limit of the neutron absorption (*13*). Trace amounts of Sm and Gd, which have extremely high neutron-absorption cross sections, may also be present. Although the large size of most of the XRS footprints on Mercury's surface makes direct correlation of the present results with identified geological units difficult, we note that the highest Mg/Si, Ca/Si, and S/Si ratios are found in areas that include substantial amounts of low-reflectance material, supporting the possibility that sulfides contribute to the low reflectance.

References and Notes

1. S. C. Solomon *et al.*, *Planet. Space Sci.* **49**, 1445 (2001).
2. H. T. Howard *et al.*, *Science* **185**, 179 (1974).
3. D. M. Hunten, D. E. Shemansky, T. H. Morgan, C. R. Chapman, M. S. Matthews, "The Mercury atmosphere," in *Mercury,* F. Vilas, C. R. Chapman, M. S. Matthews, Eds. (Univ. Arizona Press, Tucson, AZ, 1988), pp. 562–612.
4. S. C. Solomon, *Earth Planet. Sci. Lett.* **216**, 441 (2003).
5. B. W. Denevi, M. S. Robinson, *Icarus* **197**, 239 (2008).
6. J. S. Lewis, *Annu. Rev. Phys. Chem.* **24**, 339 (1973).
7. S. J. Weidenschilling, *Icarus* **35**, 99 (1978).
8. B. Fegley Jr., A. G. W. Cameron, *Earth Planet. Sci. Lett.* **82**, 207 (1987).
9. W. W. L. Benz, W. L. Slattery, A. G. W. Cameron, *Icarus* **74**, 516 (1988).
10. W. Benz, A. Anic, J. Horner, J. A. Whitby, *Space Sci. Rev.* **132**, 189 (2007).
11. G. J. Taylor, E. R. D. Scott, in *Meteorites, Comets, and Planets*, A. M. Davis, Ed., vol. 1 of *Treatise on Geochemistry*, H. D. Holland, K. K. Turekian, Eds. (Elsevier-Pergamon, Oxford, UK, 2003), pp. 477–485.
12. C. E. Schlemm II *et al.*, *Space Sci. Rev.* **131**, 393 (2007).
13. Details of analysis methods are available as supporting material on *Science* Online.
14. P. E. Clark, J. I. Trombka, *J. Geophys. Res.* **102**, 16361 (1997).
15. L. R. Nittler *et al.*, *Meteorit. Planet. Sci.* **36**, 1673 (2001).
16. J. W. Head *et al.*, *Science* **333**, 1853 (2011).
17. A. L. Sprague *et al.*, *Planet. Space Sci.* **57**, 364 (2009).
18. P. Wurz *et al.*, *Planet. Space Sci.* **58**, 1599 (2010).
19. R. Rieder *et al.*, *Science* **278**, 1771 (1997).
20. B. Fegley Jr., in *Meteorites, Comets, and Planets*, A. M. Davis, Ed., vol. 1 of *Treatise on Geochemistry*, H. D. Holland, K. K. Turekian, Eds. (Elsevier-Pergamon, Oxford, UK, 2003), pp. 487–507.
21. P. H. Warren, *Annu. Rev. Earth Planet. Sci.* **13**, 201 (1985).

22. S. M. Brown, L. T. Elkins-Tanton, *Earth Planet. Sci. Lett.* **286**, 446 (2009).
23. M. S. Robinson, G. J. Taylor, *Meteorit. Planet. Sci.* **36**, 841 (2001).
24. P. N. Peplowski *et al.*, *Science* **333**, 1850 (2011).
25. J. W. Morgan, E. Anders, *Proc. Natl. Acad. Sci. U.S.A.* **77**, 6973 (1980).
26. T. H. Burbine *et al.*, *Meteorit. Planet. Sci.* **37**, 1233 (2002).
27. T. J. McCoy, T. L. Dickinson, G. E. Lofgren, *Meteorit. Planet. Sci.* **34**, 735 (1999).
28. A. L. Sprague, D. M. Hunten, K. Lodders, *Icarus* **118**, 211 (1995).
29. L. Kerber *et al.*, *Earth Planet. Sci. Lett.* **285**, 263 (2009).
30. D. T. Blewett *et al.*, *Science* **333**, 1856 (2011).
31. B. W. Denevi *et al.*, *Science* **324**, 613 (2009).
32. M. S. Robinson *et al.*, *Science* **321**, 66 (2008).
33. D. S. Ebel, C. M. O'D. Alexander, *Planet. Space Sci.*, 10.1016/j.pss.2011.07.017 (2011).
34. D. J. Lawrence *et al.*, *Icarus* **209**, 195 (2010).
35. K. Lodders, B. Fegley, *The Planetary Scientist's Companion* (Oxford Univ. Press, New York, 1998).
36. J. J. Papike, G. Ryder, C. K. Shearer, in *Planetary Materials*, J. J. Papike, Ed., vol. 36 of *Reviews in Mineralogy*, P. H. Ribbe, Ed. (Mineralogical Society of America, Washington, DC, 1998), pp. 5-1–5-234.

Acknowledgments: We thank the MESSENGER team for the development, cruise, orbit insertion, and Mercury orbital operations of the MESSENGER spacecraft. The NASA Discovery Program under contract NAS5-97271 to The Johns Hopkins University Applied Physics Laboratory and NASW-00002 to the Carnegie Institution of Washington supports the MESSENGER mission to Mercury. Several of the authors are supported by NASA's MESSENGER Participating Scientist Program.

Supporting Online Material
www.sciencemag.org/cgi/content/full/333/6051/1847/DC1
Materials and Methods
SOM Text
Figs. S1 to S8
Table S1
References (*37–60*)

22 July 2011; accepted 31 August 2011
10.1126/science.1211567

Radioactive Elements on Mercury's Surface from MESSENGER: Implications for the Planet's Formation and Evolution

Patrick N. Peplowski,[1]* Larry G. Evans,[2] Steven A. Hauck II,[3] Timothy J. McCoy,[4] William V. Boynton,[5] Jeffery J. Gillis-Davis,[6] Denton S. Ebel,[7] John O. Goldsten,[1] David K. Hamara,[5] David J. Lawrence,[1] Ralph L. McNutt Jr.,[1] Larry R. Nittler,[8] Sean C. Solomon,[8] Edgar A. Rhodes,[1] Ann L. Sprague,[5] Richard D. Starr,[9] Karen R. Stockstill-Cahill[4]

The MESSENGER Gamma-Ray Spectrometer measured the average surface abundances of the radioactive elements potassium (K, 1150 ± 220 parts per million), thorium (Th, 220 ± 60 parts per billion), and uranium (U, 90 ± 20 parts per billion) in Mercury's northern hemisphere. The abundance of the moderately volatile element K, relative to Th and U, is inconsistent with physical models for the formation of Mercury requiring extreme heating of the planet or its precursor materials, and supports formation from volatile-containing material comparable to chondritic meteorites. Abundances of K, Th, and U indicate that internal heat production has declined substantially since Mercury's formation, consistent with widespread volcanism shortly after the end of late heavy bombardment 3.8 billion years ago and limited, isolated volcanic activity since.

Measurements of the surface composition of Mercury offer a special window into the epoch of planet formation in the inner solar system. Mercury likely preserves a more complete record of early crustal formation than do Venus, Earth, or Mars, each of which experienced extensive and prolonged resurfacing and near-surface alteration since earliest crustal formation. The MESSENGER spacecraft, inserted into orbit about Mercury on 18 March 2011, carries a suite of instruments designed for elemental and mineralogical remote sensing. We report abundances of radioactive elements on the surface of Mercury that we determined from measurements with MESSENGER's Gamma-Ray Spectrometer (GRS).

The MESSENGER GRS measures 0.25- to 9-MeV gamma rays originating from isotope-specific gamma-ray emission from the surface (*1*). The two sources of gamma-ray emission are natural radioactive decay of unstable elements (e.g., K, Th, U) and excitation of stable elements (e.g., Si, O, Fe, Ti, S, Ca) by incident galactic cosmic rays. This work focuses on measurements of the elemental abundances of K, Th, and U through the detection of gamma rays emitted during the decay of the naturally occurring radioactive isotopes ^{40}K, ^{232}Th, and ^{238}U. MESSENGER's highly eccentric orbit, combined with the altitude dependence of the gamma-ray signal, limits GRS compositional measurements to the region northward of ~20° S latitude. GRS compositional data nonetheless cover a variety of geologic terrain types, including heavily cratered terrain and smooth plains (*2*, *3*). The data discussed here were acquired at low altitudes (<2000 km) during the first Mercury sidereal day (~59 Earth days) of orbital operations (*4*). To improve the statistical significance of the results, the low-altitude data were summed to create a single data set covering the measured region. The resulting GRS measurements of surface elemental abundances therefore should be regarded as representative values for this region.

Count rates of gamma rays emanating from the surface are obtained by fitting the peaks of interest in the gamma-ray energy spectra (Fig. 1) for the summed low-altitude measurements and correcting for the background gamma-ray count rates derived from a summed high-altitude (>14,000 km) data set. These count rates have been compared, for each spectral peak, to count rates in the detector derived from calculated surface gamma-ray fluxes to determine the elemental abundance required to account for the measured signal (*4*). The average surface abundances of radioactive elements on the surface of Mercury north of ~20°S are 1150 ± 220 parts per million (ppm) K, 220 ± 60 parts per billion (ppb) Th, and 90 ± 20 ppb U. The quoted errors represent the 1-SD statistical uncertainties of the measurements, as well as the systematic uncertainties introduced during the conversion of measured count rates to surface elemental abundances.

Ratios of the moderately volatile incompatible element K to the refractory incompatible elements Th and U provide insights into the volatile inventory of planetary bodies. In contrast, the absolute abundances of these elements can vary appreciably over a planetary surface as a result of variations in melt generation and crustal emplacement and modification processes. Mercury's K/Th ratio is 5200 ± 1800, a value comparable to those for the other terrestrial planets, which range from 2000 to 7000 (*5*, *6*). By contrast, the lunar K/Th value (360) is an order of magnitude lower (*7*), indicative of the depletion of lunar volatiles relative to those of Earth. Mercury's K/Th ratio indicates that the planet's volatile budget relative to refractory elements is similar to that of the other terrestrial planets.

---

[1] The Johns Hopkins University Applied Physics Laboratory, Laurel, MD 20723, USA. [2] Computer Sciences Corporation, Lanham-Seabrook, MD 20706, USA. [3] Department of Geological Sciences, Case Western Reserve University, Cleveland, OH 44106, USA. [4] National Museum of Natural History, Smithsonian Institution, Washington, DC 20013, USA. [5] Lunar and Planetary Laboratory, University of Arizona, Tucson, AZ 85721, USA. [6] Hawaii Institute of Geophysics and Planetology, University of Hawaii, Honolulu, HI 98622, USA. [7] Department of Earth and Planetary Science, American Museum of Natural History, New York, NY 10024, USA. [8] Department of Terrestrial Magnetism, Carnegie Institution of Washington, Washington, DC 20015, USA. [9] Physics Department, The Catholic University of America, Washington, DC 20064, USA.

*To whom correspondence should be addressed. E-mail: patrick.peplowski@jhuapl.edu

Science AAAS

Supporting Online Material for

The Major-element Composition of Mercury's Surface from MESSENGER X-ray Spectrometry

Larry R. Nittler, Richard D. Starr, Shoshana Z. Weider, Timothy J. McCoy, William V. Boynton, Denton S. Ebel, Carolyn M. Ernst, Larry G. Evans, John O. Goldsten, David K. Hamara, David J. Lawrence, Ralph L. McNutt, Jr., Charles E. Schlemm II, Sean C. Solomon, Ann L. Sprague

.

correspondence to: lnittler@ciw.edu

This PDF file includes:

- SOM Text
- Figs. S1 to S8
- Table S1
- References (37-60)

1. MESSENGER X-Ray Spectrometer Data

The MESSENGER X-Ray Spectrometer (XRS) consists of three gas-filled proportional counter (GPC) detectors and a solar-pointing Si-PIN photodiode detector (Solar Assembly for X-rays, or SAX) (*12*). The energy range for all the detectors is ~1 – 10 keV. The energy resolution of the GPCs is insufficient to resolve the fluorescent K_α lines of the geochemically important elements Mg, Al, and Si (at 1.25, 1.49, and 1.74 keV, respectively). A "balanced filter" approach is therefore employed, in which thin foils of Mg and Al placed in front of two of the detectors provide selective absorption at different energies and allow the fluorescent signals from these elements to be deconvolved (*37, 38*). Elements of higher atomic number (e.g., S, Ca, Ti, Fe) can be sufficiently resolved without such filtering.

While MESSENGER orbits Mercury, the XRS continuously collects spectra from all four detectors along with ancillary engineering data (e.g., detector temperatures). Integration times vary along the orbit; the shortest times (40 s for the time period discussed here) occur near perihelion and the longest (450 s) when the spacecraft is far from the planet. GPC spectra contain a number of separate signals, including: (1) background counts due to galactic cosmic-ray interactions with the detector gas, (2) characteristic fluorescent X-rays from the planet, (3) scattered solar X-rays, and (4) pulses due to interactions with energetic electrons in the magnetosphere (*39, 40*). During typical non-flaring ("quiet Sun") conditions, the solar X-ray flux induces measurable fluorescence from the planet only up to an energy of ~2 keV (including Mg, Al, and Si). When the flux of X-rays from the Sun increases during solar flares, especially at higher energies (i.e., the spectrum "hardens'), a more intense fluorescence spectrum is produced and elemental lines up to Fe K_α (6.4 keV) can be detected. Figure S1 shows example SAX spectra and GPC spectra for a quiet-Sun integration and a single spectral integration during a solar flare. Electron-induced signals are clearly identified (Fig. S2) by the presence of fluorescence from the Al and Mg filters, Cu fluorescence from the Be-Cu collimator in front of the GPCs, and a distinctive Bremsstrahlung continuum.

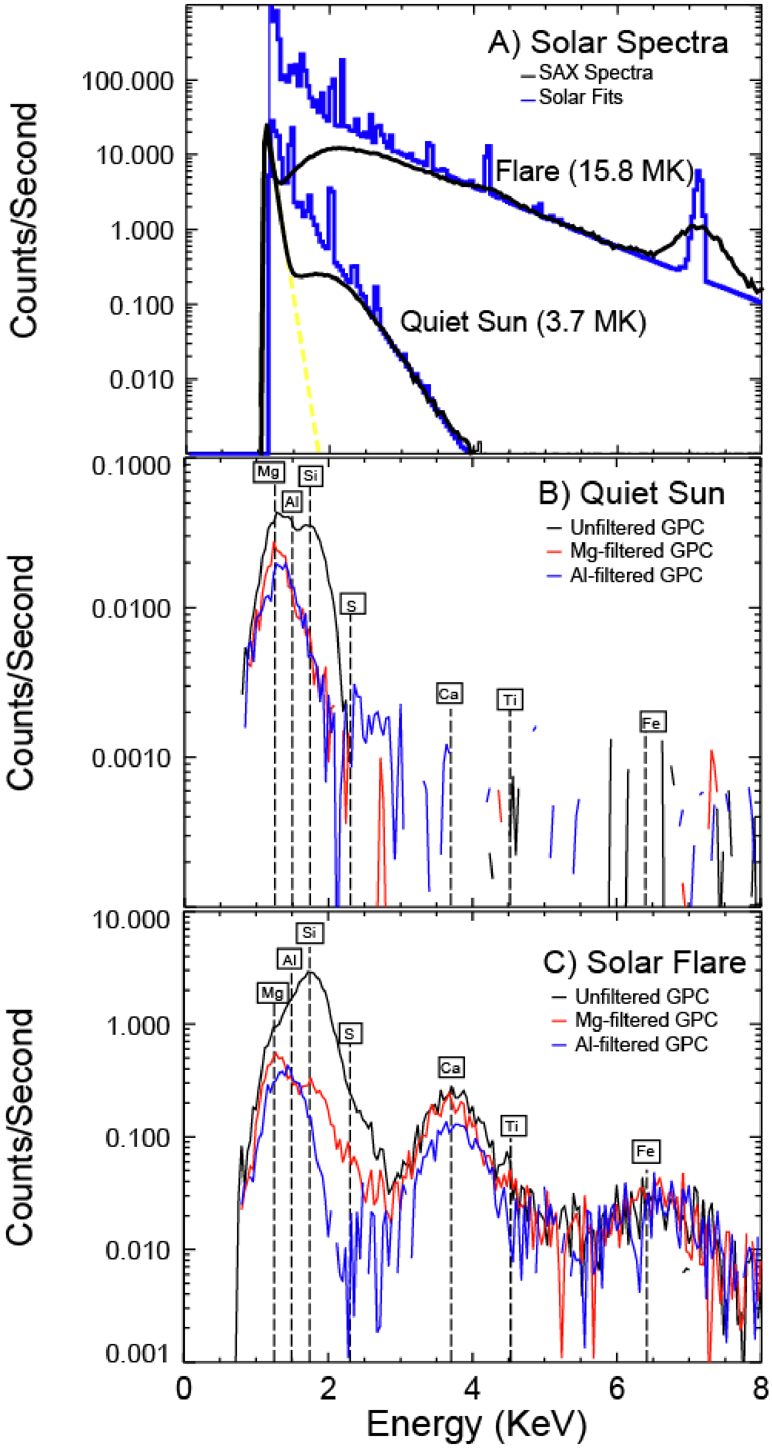

Fig. S1. (**A**) Observed solar (SAX) spectra acquired during a solar flare on 1 May 2011 and a period of "quiet-Sun" activity. The dashed yellow line indicates the electronic background in the detector. Blue curves are theoretical solar spectra that best fit the observed data when convolved with the instrument response (see Fig. S3). Plasma temperatures for the two fits are indicated. The flare spectrum has higher intensity, especially at higher energies. (**B**) Background-subtracted GPC spectra observed from Mercury during the quiet-Sun period (~32,000-s integration) from panel (A). (**C**) Same as (B), but for a 450-s integration during the 1 May solar flare. The energies of K_α fluorescent lines of major elements are labeled and indicated by the vertical dashed lines.

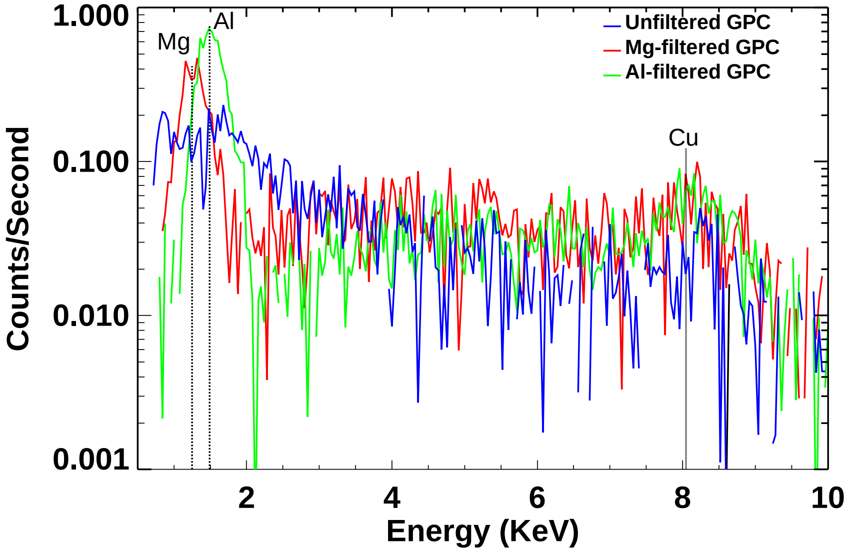

Fig. S2. Background-subtracted GPC spectra caused by interactions with energetic electrons in Mercury's magnetosphere. Fluorescence of the Mg and Al filters and the Be-Cu collimator are visible as well as a Brehmstrallung-induced continuum.

As discussed in the main text, this paper focuses on solar flare data because they provide the most complete set of geochemical data. Most of the flare data presented in this paper (Tables 1 and S1) were selected because they were acquired during the largest solar flares witnessed by XRS as of this writing. They therefore contain the highest levels of flux, including signals for elements heavier than Si: S, Ca, Ti and Fe. The analysis has been limited to those periods where there are at least three consecutive spectra that contain a substantial Ca signal and no spectral contamination from electrons or other energetic particles. The 1 May 2011 flare had particularly high fluorescent signal and was thus included, despite consisting of only two spectral integrations. For each flare, individual spectral integrations were analyzed separately and the resulting abundance ratios then averaged to provide the mean values given in Table 1. The flare on 16 April 2011 occurred close to perihelion and provided measurements of better spatial resolution than the rest of this dataset. The shorter spectral integration times gave poorer signal-to-background ratios and meant that some of the individual spectra had to be summed prior to analysis for this flare. Moreover, the last two spectra acquired during this flare were obtained from a region with geologically distinct material *(16)*, and we thus report a separate average for these two integrations and the earlier part of the flare.

For some of the flares, the analysis revealed inconsistent geochemical results for spectra acquired during the initial, pre-peak stage of the flare and those acquired following the peak flare intensity. Garcia (*41*) showed that during the early stages of a solar flare the X-ray emitting plasma is multi-thermal in nature; after the peak has been reached a more isothermal regime dominates. Our modeling approach (see below) is based on the assumption that the emitting plasma is isothermal. Therefore we infer that the aberrant results found in some pre-peak spectra are because this assumption was incorrect. For these flares, we use data only from integrations that occur at, or following, the flare peak (in terms of plasma temperature) to calculate the mean values in Table 1.

The number of analyzed integration periods is given along with geometric information for each flare in Table S1.

Average incidence, emission, and phase angles for each XRS integration are calculated by averaging those derived for sub-regions of the instrument footprint on the planet's surface. These footprints are derived from the spacecraft viewing geometry and a shape model of Mercury. The values given in Table S1 are further averaged over the separate integrations during each flare.

2. XRS Data Analysis

2.1. Fluorescence and scatter models

We use an analytical ("fundamental parameters") approach (*14*, *15*, *42*) to calculate theoretical fluorescence and coherent scattered spectra with which to compare our observed XRS spectra. For a flat, chemically homogeneous sample and an incident X-ray spectrum, $J_0(E)$, the intensity of fluorescent X-rays for element *i* emitted from the sample is given by (*14*)

$$I_i = C_i \; \omega_i \; \frac{r_j - 1}{r_j} \; \frac{\mathrm{d}\Omega}{4\pi} \int_{E_{edge}}^{E_{Max}} \frac{J_0(E) \; \mu_i(E)}{\sum_{j=1}^{n} C_j \; \left(\mu_j(E) + \mu_j(E_i) \frac{\cos(\alpha)}{\cos(\beta)}\right)} \, \mathrm{d}E \qquad (1)$$

where C_i is the concentration of element *i*, $\mu_i(E)$ is the mass-absorption coefficient for element *i* at energy *E*, α is the incidence angle (with respect to the surface normal), β is the emission angle (with respect to the surface normal), ω_i is the fluorescence probability for element *i*, r_j is the "jump ratio" for element *i* (change in mass absorption coefficient across absorption edge), E_i is the fluorescent line energy for element *i*, and dΩ is the differential solid angle viewed by the detector. The integration is taken from the absorption edge (i.e., any incident photon with energy higher than this value can induce fluorescence) to a maximum value beyond which any additional contribution to the integral is negligible ($E_{max} = 20$ keV here). This equation shows that the fluorescence intensity of a given element depends on a number of factors, including the measurement geometry and the total composition (i.e., the proportions of constituent elements) of the sample. For example, the sum in the denominator within the integral is over all elements in the sample, which means that the fluorescence signal of any element depends on all the other elements present. Therefore, the measured fluorescent X-ray intensity cannot be related to elemental composition in a straightforward manner.

In addition to fluorescence from surface atoms, MESSENGER XRS spectra also contain solar X-rays scattered from the surface into the detectors. We consider only coherent (Thomson) scattering for this work; incoherent (Compton) scattering is expected to be negligible. We use a model similar to that used by Clark and Trombka (*14*) to calculate the intensity of scattered X-rays at energy *E* and scatter (phase) angle θ:

$$I_{scatt}(E,\theta) = 0.0239 \; (1 + \cos^2(\theta)) \; J_0(E) \; \frac{\sum_{j=1}^{n} \frac{C_j}{W_j} \; f_j^2(E,\theta)}{\sum_{j=1}^{n} C_j \mu_j(E)(1 + \frac{\cos(\alpha)}{\cos(\beta)})} \times \mathrm{d}\Omega \quad (2)$$

In this equation, the sums are over all elements in the sample, W_j is the atomic weight of element *j*, f_j is the "atomic structure factor" for element *j*, and the other factors are the same as discussed above for fluorescence (Eq. 1). For this work, mass-absorption coefficients are taken from the NIST database (*43*) and structure factors from Hubbell *et al.* (*44*). Ideally, the phase-angle dependence means that Eq. 2 should be integrated over the solid angle of the instrument field of view for each spectral integration before combining with the predicted fluorescence from Eq. 1. However, in practice, this step is not straightforward; instead we have empirically determined that the predicted scattered flux should be multiplied by a factor of 0.8 before adding in the predicted fluorescence intensity. This factor results in good fits to the XRS spectra as described below.

2.2. Solar monitor fitting

The above equations show that knowledge of the incident solar X-ray spectrum is essential for relating observed XRS spectra to elemental abundances on Mercury. For each observation, the shape of the solar spectrum is derived by fitting the observed solar (SAX) spectrum with a theoretical isothermal solar plasma spectrum that has been generated with the *Chianti* code (*45*) and then convolved with the SAX instrument response function. The fitting is accomplished via a non-linear χ^2-minimization routine, written in the IDL language (ITT) that makes use of routines in the SolarSoft (*46*) and MPFIT libraries (*47*). The free parameters in the fit include the absolute scale of the spectrum (related to the volume of emitting plasma, or emission measure, as well as the solid angle of the detector), the plasma temperature, the magnitude of the electronic detector background, and the elemental abundances of the emitting plasma.

The electronic background manifests itself as a power-law signal at low channels (Fig. S1). The power-law index (~ −0.2) is derived from quiet-Sun SAX spectra acquired on the same day as a given flare, but the magnitude of the background signal can be varied in the fit. Elemental fractionation in the solar corona has long been recognized (*48*); abundances of elements with a high first ionization potential (FIP >~10 eV) are systematically lower than those with lower first ionization potentials, relative to photospheric abundances. In addition, solar flare observations indicate temporal variability in the abundances of many elements in the coronal plasma (*49*). In the SAX flare spectral-fitting routine, we vary the abundances of low-FIP elements (e.g., Na, Mg, Al, Si) as a group, relative to their nominal average coronal abundances (*50*), and independently vary S, Ca, and Fe. During large flares, Ca and Fe line complexes are visible in the SAX spectra. S lines are not clearly visible, but S emission is very close to the turn-over in the SAX spectrum at ~2 keV (Fig. S1) owing to absorption by the thin Be window in front of the detector. Thus, we have found that the shape of the SAX spectrum at around ~2 keV is quite sensitive to the assumed elemental abundances in the coronal plasma. For the data reported here, best-fit coronal abundances are consistent with ranges seen in previous studies. An example fit to a SAX spectrum is shown in Fig. S3. The best-fit plasma parameters for an observed SAX spectrum are used to generate a corresponding high-energy-resolution spectrum (Fig. S1A) as an input for the fluorescence and scatter models used to fit the XRS spectra.

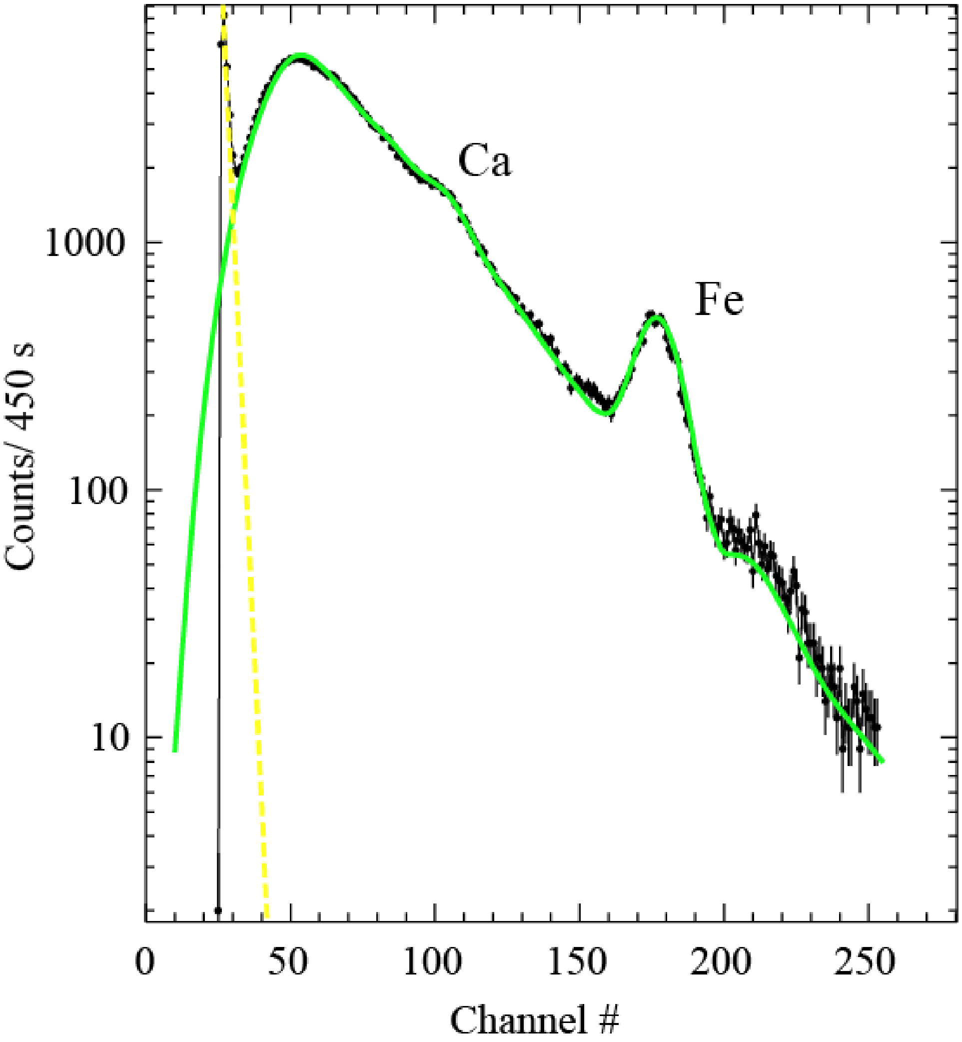

Fig. S3. Example fit to a SAX spectrum acquired during a large solar flare on 1 May 2011. Black dots with one-standard-deviation statistical error bars are the observed spectrum. The dashed yellow line is the electronic background in the detector; the green curve is the best-fit (15.8 MK plasma temperature) solar spectrum convolved with instrument response. See Fig. S1A for the higher-resolution solar spectrum corresponding to this fit. The positions of observable line complexes from Ca and Fe are indicated.

2.3. Background subtraction

The GPC spectra contain a background due to galactic cosmic-ray and solar energetic particle interactions with the detectors. The overall shape of the background spectrum in each detector is fairly constant over the timescale of a day, but the absolute normalization varies, most likely due to variable shielding of the detectors from some of the particle flux by Mercury itself as the spacecraft orbits the planet in its highly elliptical orbit. For the spectra analyzed here, the background in each detector was taken as the sum of all spectra acquired within approximately a day of the flare and for which the instrument field of view did not overlap with the sunlit planet. For fitting, the background normalization was either fixed such that the background matched the foreground spectrum at the highest channels (> ~8 keV where no fluorescence or scattered solar signal is expected) or, in some cases, allowed to freely vary during the fit procedure (see below).

2.4. Planetary spectral fitting: elemental abundance determination

Once an appropriate solar spectrum and background GPC spectra have been determined for a given XRS integration period, the GPC spectra are fit in order to obtain elemental abundances. We use a non-linear χ^2 minimization routine in which theoretical GPC spectra are repeatedly generated and compared to the observed spectra, with elemental abundances varied until the best fit is obtained. The fitting program is implemented in IDL and uses the MPFIT library (*47*). A similar approach was recently developed to analyze data from the C1XS instrument on the lunar Chandrayaan-1 mission (*51-53*). Typical surface materials on the terrestrial planets show a relatively limited range in Si content, so in order to help ensure convergence of the fit, we fix the relative abundance of Si and vary the abundances of the other major elements in the energy range of the XRS (Mg, Al, S, Ca, Ti, Cr, Mn, and Fe), relative to this value. However, a major portion (>40 wt%) of typical planetary materials consists of O, which cannot be measured by the XRS. Hence, the fitting algorithm assigns an O abundance on the basis of typical oxide stoichiometry for cations (e.g., two O atoms for every Si atom) and renormalizes the overall composition to 100%.

In addition to the elemental abundances, the fitting parameters also include an overall normalization parameter, the energy calibration (keV/channel and energy at channel zero) of each detector, and the normalization of the cosmic-ray-induced background in each detector (previous section). For each iteration of the fitting routine, Eqs. 1 and 2 are used to calculate fluorescence and scattered solar spectra for the given input solar spectrum and appropriate geometrical parameters (Table S1). These spectra are then added and convolved with the instrument response to generate synthetic spectra for the three GPC detectors independently. The synthetic spectra include escape peaks but ignore possible fluorescence of the Mg and Al filters, as this is calculated to be negligible. The synthetic spectra are compared to the observed spectra, providing a χ^2 value, and new parameters are chosen for the next iteration. The process is repeated until a minimum χ^2 value is found.

Example fits to the three GPC spectra are shown in Fig. S4 for a single integration during the 1 May 2011 flare (see Figs. S1 and S3, Tables 1 and S1). The same fit is shown in Fig. S5, but there the three (background-subtracted) GPC spectra and corresponding best-fit synthetic spectra are summed to improve the signal-to-noise ratio at high energy. In Fig. S5 the scattered solar component of the best-fit spectrum is also indicated. The effect of varying the abundances of S, Ti, and Fe, relative to Si, on the shape of the synthetic spectrum is illustrated in Fig. S6, which thus shows the sensitivity of the XRS flare spectra to these elements.

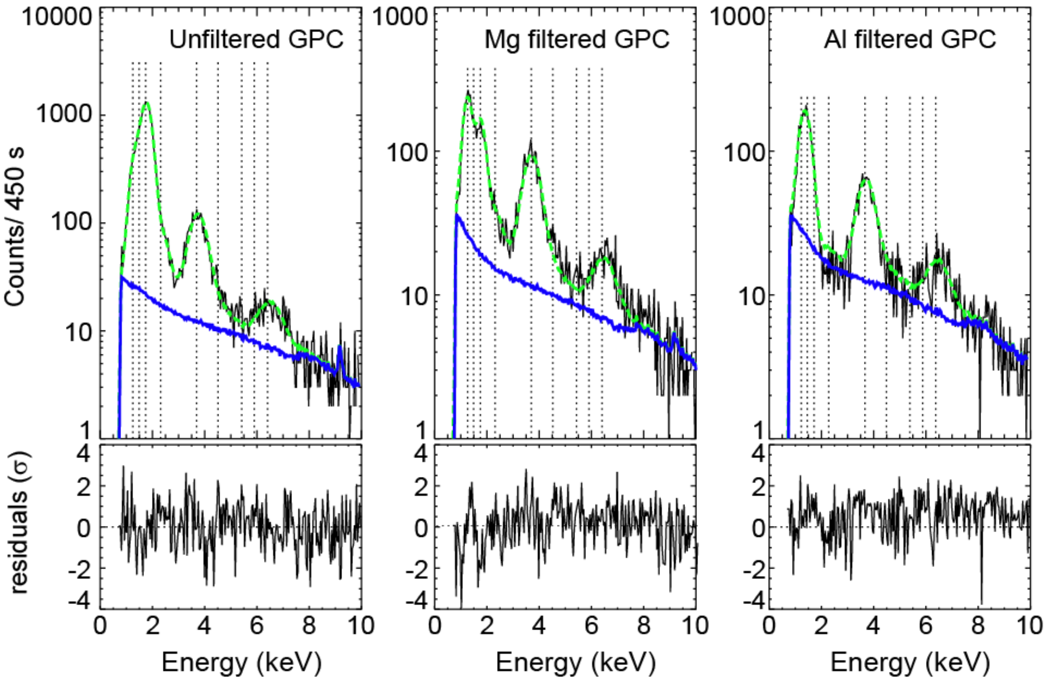

Fig. S4. Example fits to GPC spectra acquired during the 1 May 2011 flare (see Figs. S1A and S3 for the corresponding solar spectrum). Solid black lines in the top panels are the observed spectra. Green dashed lines are best-fit synthetic spectra, and blue lines are appropriately scaled cosmic-ray-induced background. Dashed vertical lines indicate locations of K_α lines of (left to right) Mg, Al, Si, S, Ca, Ti, Cr, Mn, and Fe. Bottom panels indicate the fit residuals.

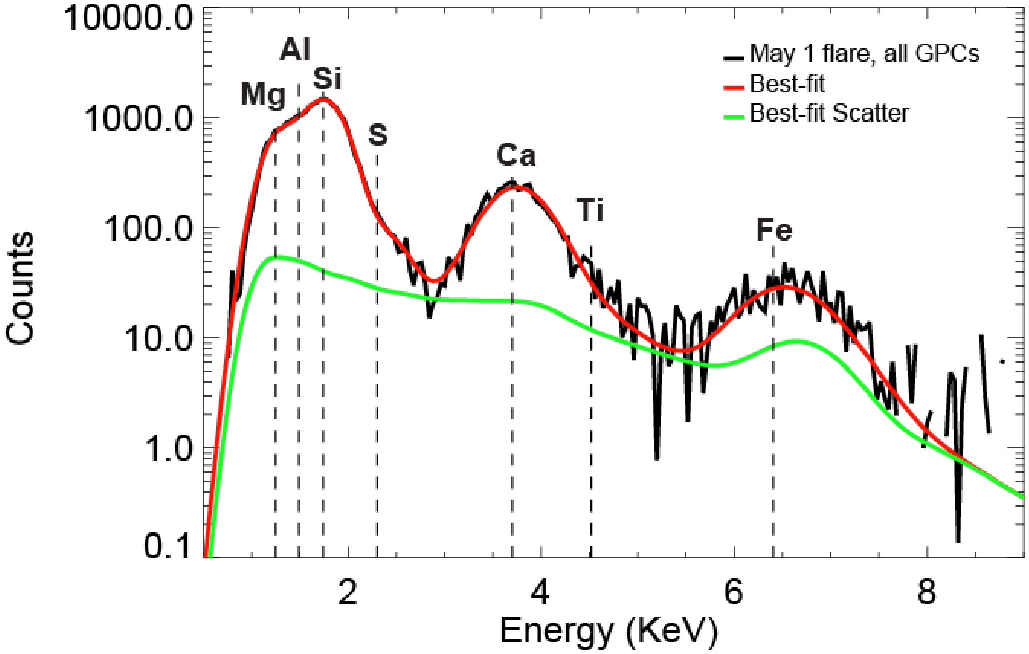

Fig. S5. Spectrum of the 1 May 2011 flare (sum of the three GPC detectors, 450-s integration) with best-fit synthetic spectrum. Red curve is the best-fit spectrum; green curve is the scattered solar component.

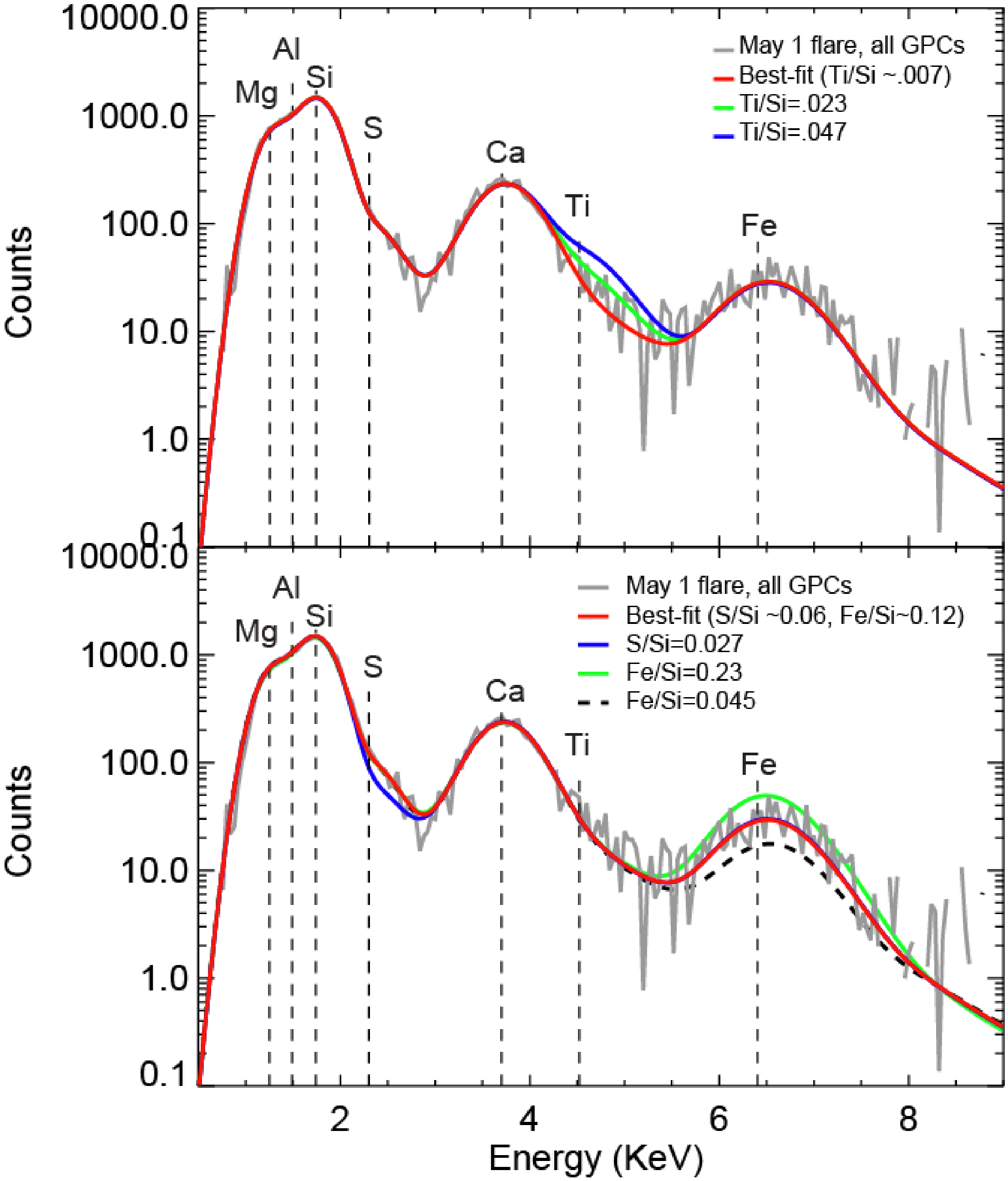

Fig. S6. Spectrum of the 1 May 2011 flare (sum of the three GPC detectors) with synthetic spectra. Red curve is the best-fit spectrum from Fig. S5. The other colors indicate the effect of varying the S, Ti, or Fe abundance in the modeling.

K_α fluorescent X-ray emission for Cl occurs at 2.622 keV, just above the S line at 2.308 keV. Thus, if sufficient Cl were present, it would be observable as a shoulder on the S line. No such shoulder was visible in any of the XRS flare spectra analyzed here. To estimate an upper bound on the surface Cl abundance, we re-fit the 1 May 2011 flare (e.g., Figs. S4-S6) GPC data, fixing the abundances of Mg, Al, Si, S, Ca, and Fe to their best-fit values and varying the Cl abundance. This procedure resulted in a best-fit Cl/Si ratio of 0.014 ± 0.033, from which we estimate a 2-standard-deviation upper limit of 0.008, or Cl < ~0.2 wt%.

Abundances of Mn (K_α = 5.898 keV) and Cr (K_α = 5.414 keV) were varied as part of the fitting procedure described above for all the largest flare spectra, but these elements were not unambiguously identified. From the fit uncertainties for the largest flare spectra, we estimated conservative upper bounds of ~0.5 wt% for these elements.

2.5. Systematic errors

Statistical errors for individual measurements are derived from the fitting procedure. Systematic uncertainties due to incorrect background subtraction, incompletely understood solar incident spectra, and invalid assumptions in the fundamental parameters of the model are certainly larger than the statistical errors (likely to be up to tens of percent, relative) and are discussed here.

Background subtraction. As discussed above, the shape of the particle-induced background in the GPC detectors is relatively constant over a ~1-day timescale, but the absolute normalization varies. We have analyzed the flare spectra both by fixing the background component so that it matches the observed spectra above ~8 keV and by allowing the scale of the background in each detector to be varied as free parameters during the least-squares fitting. Both approaches give similar results for the major-element ratios Mg/Si, Al/Si, S/Si, and Ca/Si, but the elements with lower absolute abundances and/or higher fluorescent energies (Ti, Cr, Mn, and Fe) are more sensitive to the details of the background scaling. For example, fitting the 1 May 2011 flare spectra with normalized backgrounds in the three detectors (as in Fig. S4) gives Ti/Si = 0.007 ± 0.003 and Fe/Si = 0.12 ± 0.01. When the background scaling is allowed to float freely during the fitting routine for the same spectra, the results are different: Ti/Si = 0.016 ± 0.003 and Fe/Si = 0.15 ± 0.01 (representing an increase of >100% and 25%, respectively). As a result, we believe that the quantitative abundance ratio values derived for these elements from the analyzed flares are still highly uncertain, but the upper limits we report in the main text are conservative. This situation will improve with our understanding of the detector background, but these abundance ratios are also subject to other systematic uncertainties discussed below.

Solar fitting. The SAX-fitting procedure is based on the assumption that the incident solar spectrum over the time of an XRS integration is accurately described by an isothermal plasma model. However, during flares the plasma temperature can change rapidly and to some extent is multi-thermal, especially in the earliest stages (*41*). Additional errors in the solar spectra fitting are introduced by the poor energy resolution and low efficiency at low energy of the SAX detector, especially since individual lines in the spectrum cannot be resolved. The accuracy of the fitted solar spectra (Fig. S3) suggests that the isothermal approximation is valid. In fact, the fits are worse when two temperatures are used to fit the flare spectra, as was the procedure for the NEAR XRS analysis (*54*). Nonetheless, errors in solar fitting will lead directly to errors in derived elemental abundance ratios. By examining the spectrum-to-spectrum variability in the derived abundance ratios for a given solar flare analysis, the magnitude of errors introduced by incorrect solar spectra modeling can be estimated. For example, Fig. S7 shows the Mg/Si, Al/Si, S/Si, and Ca/Si ratios derived for individual spectra plotted against inferred plasma temperature for our analyzed flares. Each flare shows spectrum-to-spectrum variation in the abundance ratios as a function of temperature, indicating that there are residual errors in the analysis methodology, almost certainly due to errors in the solar fitting. However, Fig. S7 demonstrates that the flare-to-flare variability is much larger than the variability within a single flare analysis, and the XRS data thus clearly reveal elemental heterogeneity on the surface of Mercury. The Mg/Si, Al/Si, S/Si, and Ca/Si ratios reported in Table 1 of the main text are the mean values and the errors the standard deviations of the individual spectra for each flare. Hence, these errors include our best estimates of the systematic uncertainty due to incorrect solar fitting and are typically 5 – 10% for these ratios.

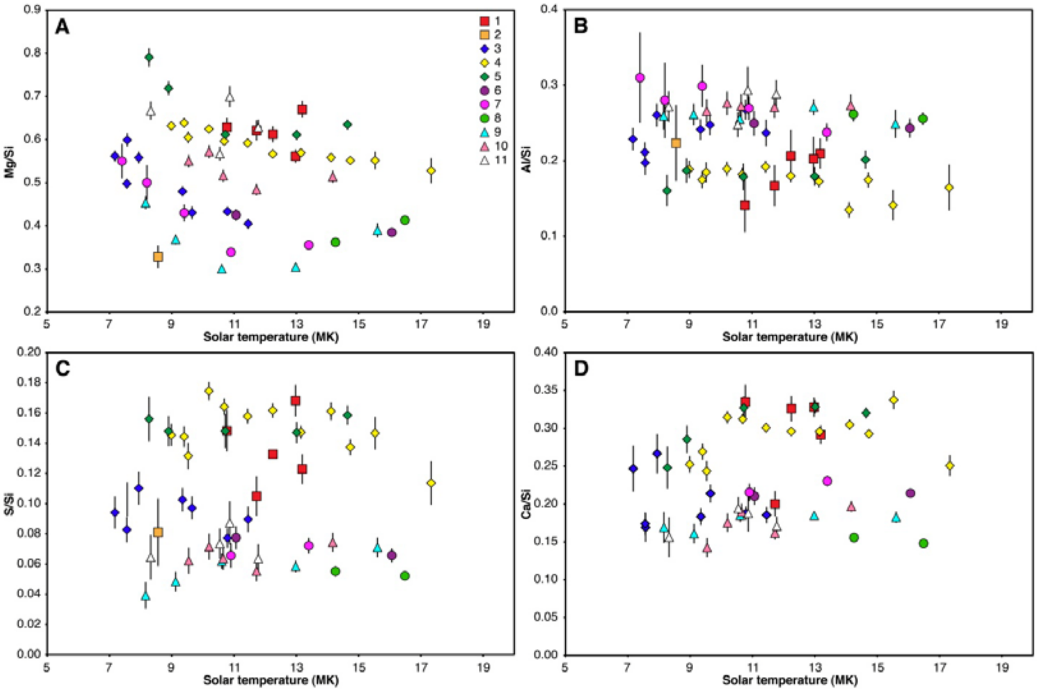

Fig. S7. Derived (A) Mg/Si, (B) Al/Si, (C) S/Si, and (D) Ca/Si ratios for individual XRS spectra plotted against inferred solar temperature. For a given flare (numbers refer to flares in Tables 1 and S1), variation in composition with temperature indicates residual errors in solar fitting. Reported errors on abundance ratios include this uncertainty. Flare-to-flare variability is clearly larger than the range of individual spectra within a single flare. Note that the second part of the 16 April flare (labeled 2) is clearly compositionally distinct from the earlier part of the flare (labeled 1). Flare 2 occurred at low altitude, and its instrument footprint is on geologically different material from those for the rest of the flare (Fig. 2 in main text).

Homogeneity. For the analytical approach used here (Eqs. 1 and 2), the sampled material is assumed to be compositionally homogeneous on the scale of the X-ray interactions with the material (tens of μm). Mercury is most likely covered in fine soils due to eons of regolith processing, so such a homogeneous approximation may be reasonable. However, such a condition is not known *a priori*, and the fact that different elements are preferentially contained in different minerals can lead to incorrect results. For example, Al is primarily contained in feldspar in planetary materials. If feldspar grains in Mercury's regolith are larger than the mean free path of the X-rays, fluorescent Al X-rays should escape more easily than predicted by Eq. 1, since feldspar contains little of the Mg that is a strong absorber of Al X-rays in the homogeneous approximation. Nittler *et al.* (*15*) and Narendranath *et al.* (*55*) have estimated the magnitude of the resulting error in Al/Si ratios derived with Eq. 1 to be up to 30% for a range of compositions. This situation would result in the overestimation of Al/Si ratios by up to ~30%, depending on the nature of Mercury's regolith. The size of this effect for other elements is less clear, but it may be of comparable magnitude for S and possibly Fe, depending on the chemical form of the Fe (*15*). Note that if such corrections are necessary, it is likely that they would affect all the data equally and thus would not affect our inference of compositional heterogeneity on Mercury.

Regolith (particle) effects. The analytical model used to derive abundances is also predicated on the basic assumption that the analyzed sample is perfectly flat, whereas in reality the surface of Mercury has topography on many scales (*e.g.*, μm-particles to km-scale craters and mountains). Both laboratory experiments and theory indicate that topographic effects on X-ray fluorescence spectra can be substantial (*51*, *56-60*). In particular, surface roughness of the same magnitude as the X-ray mean-free path (tens of μm) can induce shadowing and masking effects that influence observed fluorescence signals as a function of viewing geometry. It is difficult to directly apply these studies to our analyses, due to very different compositions and incident X-ray spectra, as well as to the relatively poorly constrained nature of Mercury's regolith (*e.g.*, grain-size, porosity) and the fact that none of them consider effects on scattered X-ray spectra. Little effect is expected for ratios of elements whose fluorescence lines are close in energy (e.g., Mg/Si, Al/Si, S/Si), but the predicted fluorescence ratios of Ca/Si, Ti/S, Fe/Si, and Fe/Ca may be higher than the analytical model by as much as 50% at high incidence and/or phase angles, depending on the physical properties of the analyzed medium (*57*, *58*). If applicable to our data, correcting for this effect would cause a decrease in the inferred abundances for these elements. In fact, our data suggest trends in Mg/Si and Ca/Si that increase with incidence angle (Tables 1 and S1) and that are opposite in sign and of larger magnitude than is suggested for these regolith effects. We attribute these variations to true chemical heterogeneity on Mercury. Repeated observations of the same planetary regions under different viewing geometries should ultimately aid in resolving whether regolith effects are important for analyzing MESSENGER XRS results. In any case, our estimates of upper limits on Ti and Fe abundances (Table 1) are not changed by this effect.

3. Elemental Ratio Correlations

As discussed in the main text, the XRS-derived Mg/Si and Ca/Si ratios are generally correlated with the S/Si ratios (Fig. S8) supporting the suggestion that Mg- and/or Ca-sulfides may be present on Mercury. The slope of the Ca/Si versus S/Si trend is ~1.3, close to the weight ratio (1.25) of Ca:S in oldhamite (CaS). On the other hand, the slope of the Mg/Si versus S/Si trend (~2.3) is steeper than that expected for mixing with pure MgS (0.75), suggesting that the increase in S is also accompanied by a systematic increase in Mg in the mafic silicates, *i.e.*, towards a more ultramafic composition.

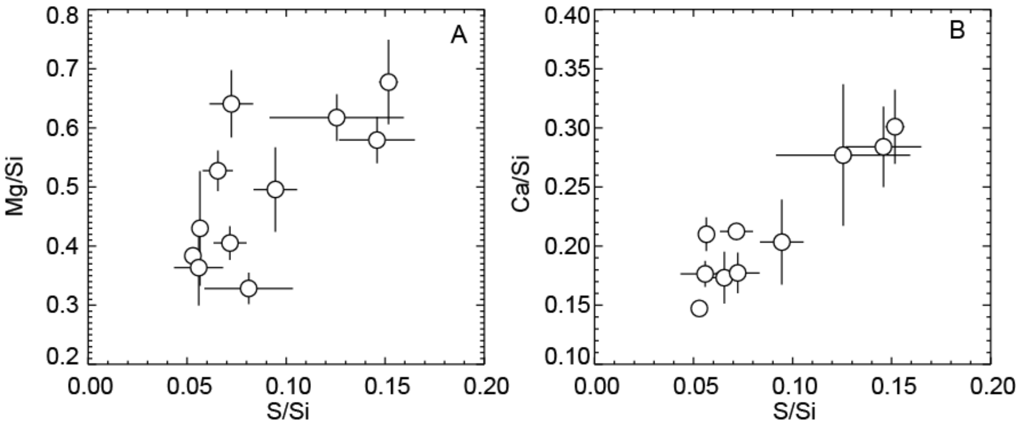

Fig. S8: Mg/Si (A) and Ca/Si (B) weight ratios plotted against S/Si weight ratios for flare analyses (data from Table 1).

Table S1.

Geometric information for analyzed solar flares

Flare	**Date in 2011 and start time (UTC)**	**Number of integrations**	**Total integration time (s)**	**Boresight latitude (°)**	**Boresight longitude (°)**	**Incidence angle (°)**	**Emission angle (°)**	**Phase angle (°)**	**Mean solar temperature (10^6 K)**
1	16 April 16:40:41	8	705	39.9	-70.6	44.6	34	78.2	12.2
2	16 April 16:53:06	2	80	65.3	-69.7	67.1	11.6	78	8.6
3	22 April 01:26:13	8	3600	-26.7	-100.1	47.3	40.8	77.5	8.9
4	22 April 04:56:47	12	2319	6.5	-53.9	17.7	62.2	76.6	12.3
5	22 April 17:01:00	5	909	2.9	-85	19.7	59.8	77.4	11.1
6	1 May 23:22:43	2	900	-50.9	-118.9	61.5	45.1	100.6	13.6
7	15 May 23:24:02	5	2250	-55.9	-133.9	58.1	46.5	100.8	9.9
8	13 June 03:53:14	2	900	-82.6	172.8	75.7	20.8	84.3	15.4
9	14 June 21:44:36	5	2250	-38.7	-101.1	73.3	23.1	83.2	11.3
10	16 June 10:19:05	5	2250	-32.7	-129.1	56.2	29.8	78.1	11.3
11	16 June 11:56:46	4	800	-14.8	-118	61.9	20.3	78.1	10.4

References and Notes

1. S. C. Solomon *et al.*, The MESSENGER mission to Mercury: Scientific objectives and implementation. *Planet. Space Sci.* **49**, 1445-1465 (2001).
2. H. T. Howard *et al.*, Mercury: Results on mass, radius, ionosphere, and atmosphere from Mariner 10 dual-frequency radio signals. *Science* **185**, 179-180 (1974).
3. D. M. Hunten, D. E. Shemansky, T. H. Morgan, C. R. Chapman, M. S. Matthews, The Mercury atmosphere. in *Mercury*, F. Vilas, C. R. Chapman, M. S. Matthews, Eds. (Univ. of Arizona Press, Tucson, AZ, 1988), pp. 562-612
4. S. C. Solomon, Mercury: The enigmatic innermost planet. *Earth Planet. Sci. Lett.* **216**, 441-455 (2003).
5. B. W. Denevi, M. S. Robinson, Mercury's albedo from Mariner 10: Implications for the presence of ferrous iron. *Icarus* **197**, 239-246 (2008).
6. J. S. Lewis, Chemistry of the planets. *Annu. Rev. Phys. Chem.* **24**, 339-352 (1973).
7. S. J. Weidenschilling, Iron/silicate fractionation and the origin of Mercury. *Icarus* **35**, 99-111 (1978).
8. B. Fegley, A. G. W. Cameron, A vaporization model for iron/silicate fractionation in the Mercury protoplanet. *Earth Planet. Sci. Lett.* **82**, 207-222 (1987).
9. Benz, W. W. L. Slattery, A. G. W. Cameron, Collisional stripping of Mercury's mantle. *Icarus* **74**, 516-528 (1988).
10. W. Benz, A. Anic, J. Horner, J. A. Whitby, The origin of Mercury. *Space Sci. Rev.* **132**, 189-202 (2007).
11. G. J. Taylor, E. R. D. Scott, Mercury. in *Meteorites, Comets, and Planets*, A. M. Davis, Ed., vol. 1 of *Treatise on Geochemistry*, H. D. Holland, K. K. Turekian, Eds. (Elsevier-Pergamon, Oxford, 2003), pp. 477-485.
12. C. E. Schlemm II *et al.*, The X-Ray Spectrometer on the MESSENGER spacecraft. *Space Sci. Rev.* **131**, 393-415 (2007).
13. Details of analysis methods are available as supporting material on *Science* Online.
14. P. E. Clark, J. I. Trombka, Remote X-ray spectrometry for NEAR and future missions: Modeling and analyzing X-ray production from source to surface. *J. Geophys. Res.* **102**, 16361 (1997).
15. L. R. Nittler *et al.*, X-ray fluorescence measurements of the surface elemental composition of asteroid 433 Eros. *Meteorit. Planet. Sci.* **36**, 1673-1695 (2001).
16. J. W. Head *et al.*, Widespread and voluminous flood volcanism in the northern lowlands of Mercury revealed by MESSENGER. *Science*, this issue (2011).

17. A. L. Sprague *et al.*, Spectral emissivity measurements of Mercury's surface indicate Mg- and Ca-rich mineralogy, K-spar, Na-rich plagioclase, rutile, with possible perovskite, and garnet. *Planet. Space Sci.* **57**, 364-383 (2009).
18. P. Wurz *et al.*, Self-consistent modelling of Mercury's exosphere by sputtering, micro-meteorite impact and photon-stimulated desorption. *Planet. Space Sci.* **58**, 1599-1616 (2010).
19. R. Rieder *et al.*, The chemical composition of Martian soil and rocks returned by the mobile Alpha Proton X-ray Spectrometer: Preliminary results from the X-ray mode. *Science* **278**, 1771-1774 (1997).
20. B. Fegley, Jr., Venus. in *Meteorites, Comets, and Planets*, A. M. Davis, Ed., vol. 1 of *Treatise on Geochemistry*, H. D. Holland, K. K. Turekian, Eds. (Elsevier-Pergamon, Oxford, 2003), pp. 487-507.
21. P. H. Warren, The magma ocean concept and lunar evolution. *Annu. Rev. Earth Planet. Sci.* **13**, 201-240 (1985).
22. S. M. Brown, L. T. Elkins-Tanton, Compositions of Mercury's earliest crust from magma ocean models. *Earth Planet. Sci. Lett.* **286**, 446-455 (2009).
23. M. S. Robinson, G. J. Taylor, Ferrous oxide in Mercury's crust and mantle. *Meteorit. Planet. Sci.* **36**, 841-847 (2001).
24. P. N. Peplowski *et al.*, Radioactive elements on Mercury's surface from MESSENGER: Implications for the planet's formation and evolution. *Science*, this issue (2011).
25. J. W. Morgan, E. Anders, Chemical composition of Earth, Venus, and Mercury. *Proc. Natl. Acad. Sci. U.S.A.* **77**, 6973-6977 (1980).
26. T. H. Burbine *et al.*, Spectra of extremely reduced assemblages: Implications for Mercury. *Meteorit. Planet. Sci.* **37**, 1233-1244 (2002).
27. T. J. McCoy, T. L. Dickinson, G. E. Lofgren, Partial melting of the Indarch (EH4) meteorite: A textural, chemical and phase relations view of melting and melt migration. *Meteorit. Planet. Sci.* **34**, 735-746 (1999).
28. A. L. Sprague, D. M. Hunten, K. Lodders, Sulfur at Mercury, elemental at the poles and sulfides in the regolith. *Icarus* **118**, 211-215 (1995).
29. L. Kerber *et al.*, Explosive volcanic eruptions on Mercury: Eruption conditions, magma volatile content, and implications for interior volatile abundances. *Earth Planet. Sci. Lett.* **285**, 263-271 (2009).
30. D. T. Blewett *et al.*, Hollows on Mercury: Evidence from MESSENGER for geologically recent volatile-related activity. *Science*, this issue (2011).
31. B. W. Denevi *et al.*, The evolution of Mercury's crust: A global perspective from MESSENGER. *Science* **324**, 613-618 (2009).
32. M. S. Robinson *et al.*, Reflectance and color variations on Mercury: Regolith processes and compositional heterogeneity. *Science* **321**, 66-69 (2008).

33. D. S. Ebel, C. M. O'D. Alexander, Equilibrium condensation from cluster-IDP enriched vapor: Implications for Mercury and enstatite chondrite origins. *Planet. Space Sci.*, 10.1016/j.pss.2011.07.017 (2011).
34. D. J. Lawrence *et al.*, Identification and measurement of neutron-absorbing elements on Mercury's surface. *Icarus* **209**, 195-209 (2010).
35. K. Lodders, B. Fegley, *The Planetary Scientist's Companion* (Oxford University Press, New York, 1998).
36. J. J. Papike, G. Ryder, C. K. Shearer, Lunar samples, in *Planetary Materials*, J. J. Papike, Ed., vol. 36 of *Reviews in Mineralogy*, P. H. Ribbe, Ed. (Mineralogical Society of America, Washington, DC, 1998), pp. 5-1–5-234.
37. I. Adler *et al.*, Apollo 15 geochemical X-ray fluorescence experiment: Preliminary report. *Science* **175**, 436-440 (1972).
38. J. I. Trombka *et al.*, The elemental composition of asteroid 433 Eros: Results of the NEAR-Shoemaker X-ray spectrometer. *Science* **289**, 2101-2105 (2000).
39. J. A. Slavin *et al.*, Mercury's magnetosphere after MESSENGER's first flyby. *Science* **321**, 85-89 (2008).
40. G. C. Ho *et al.*, MESSENGER observations of transient bursts of energetic electrons in Mercury's magnetosphere. *Science*, this issue (2011).
41. H. A. Garcia, Temperature and emission measure from GOES soft X-ray measurements. *Solar Physics* **154**, 275-308 (1994).
42. R. Jenkins, J. DeVries, *Practical X-Ray Spectrometry* (Springer-Verlag, New York, 1969).
43. J. H. Hubbell, S. M. Seltzer, Tables of x-ray mass attenuation coefficients and mass energy-absorption coefficients (version 1.4). National Institute of Standards and Technology, Gaithersburg, MD (2004); http://physics.nist.gov/xaamdi.
44. J. H. Hubbell *et al.*, Atomic form factors, incoherent scattering functions, and photon scattering cross sections. *J. Phys. Chem. Ref. Data* **4**, 471-538 (1975).
45. K. P. Dere, E. Landi, H. E. Mason, B. C. Monsignori Fossi, P. R. Young, CHIANTI - an atomic database for emission lines. *Astron. Astrophys. Suppl. Ser.* **125**, 149-173 (1997).
46. S. L. Freeland, B. N. Handy, Data analysis with the SolarSoft system. *Solar Physics* **182**, 497-500 (1998).
47. C. B. Markwardt, Non-linear least-squares fitting in IDL with MPFIT, in *Astronomical Data Analysis Software and Systems XVIII*,D. A. Bohlender, D. Durand, P. Dowler, Eds. (Astronomical Society of The Pacific, San Francisco, 2009) pp. 251-254
48. U. Feldman, K. G. Widing, Spectroscopic measurement of coronal compositions. *Space Sci. Rev.* **130**, 115-126 (2007).
49. A. Fludra, J. T. Schmelz, The absolute coronal abundances of sulfur, calcium, and iron from Yohkoh-BCS flare spectra. *Astron. Astrophys.* **348**, 286-294 (1999).

50. U. Feldman, Elemental abundances in the upper solar atmosphere. *Physica Scripta* **46**, 202-220 (1992).
51. S. Z. Weider *et al.*, Planetary X-ray fluorescence analogue laboratory experiments and an elemental abundance algorithm for C1XS. *Planet. Space Sci.*, 59, 1393-1407 (2011).
52. B. Swinyard, B. Kellett, S. Z. Weider, K. H. Joy, I. A. Crawford, C1XS spectral analysis method. in *Proceedings of the "X-ray Fluorescence Spectroscopy in Planetary Remote Sensing" Workshop,* H. Lacoste, Ed. (European Space Agency SP-687, Norrdwijk, Netherlands, 2009)
53. S. Z. Weider *et al.*, The Chandrayaan-1 X-ray spectrometer: First results. *Planet. Space Sci.*, 10.1016/j.pss.2011.08.014 (2011).
54. L. F. Lim, L. R. Nittler, Elemental composition of 433 Eros: New calibration of the NEAR-Shoemaker XRS data. *Icarus* **200**, 129-146 (2009).
55. S. Narendranath *et al.*, Lunar X-ray fluorescence observations by the Chandrayaan-1 X-ray Spectrometer (C1XS): Results from the nearside southern highlands. *Icarus* **214**, 53-66 (2011).
56. T. Okada, Particle size effect in X-Ray fluorescence at a large phase angle: Importance on elemental analysis of asteroid Eros (433). *Lunar Planet. Sci.* **35**, abstr. 1927 (2004).
57. H. Parviainen, J. Näränen, K. Muinonen, Soft X-ray fluorescence from particulate media: Numerical simulations. *J. Quantit. Spectrosc. Radiat. Transfer* **112**, 1907-1918 (2011).
58. Y. Maruyama, K. Ogawa, T. Okada, M. Kato, Laboratory experiments of particle size effect in X-ray fluorescence and implications to remote X-ray spectrometry of lunar regolith surface. *Earth Planets Space* **60**, 293-297 (2008).
59. J. Näränen *et al.*, Regolith effects in planetary X-ray fluorescence spectroscopy: Laboratory studies at 1.7-6.4 keV. *Adv. Space Res.* **44**, 313-322 (2009).
60. J. Näränen *et al.*, Laboratory studies into the effect of regolith on planetary X-ray fluorescence spectroscopy. *Icarus* **198**, 408-419 (2008).